Nano Energy 38 (2017) 526–536

Contents lists available at ScienceDirect

Nano Energy

journal homepage: www.elsevier.com/locate/nanoen

Full paper

The fractal nature of the three-phase boundary: A heuristic approach to the degradation of nanostructured solid oxide fuel cell anodes

A. Bertei[a,*], E. Ruiz-Trejo[a], K. Kareh[a], V. Yufit[a], X. Wang[b], F. Tariq[a], N.P. Brandon[a]

[a] Department of Earth Science and Engineering, Imperial College London, SW7 2AZ, UK
[b] Department of Materials, Imperial College London, SW7 2AZ, UK

ARTICLE INFO

Keywords:
Anode degradation
Coarsening
Tomography
Infiltration
Electrochemical impedance spectroscopy

ABSTRACT

Nickel/zirconia-based nanostructured electrodes for solid oxide fuel cells suffer from poor stability even at intermediate temperature. This study quantifies the electrochemical and microstructural degradation of nanostructured electrodes by combining 3D tomography, electrochemical impedance spectroscopy (EIS) and mechanistic modeling. For the first time, the electrochemical degradation of nanostructured electrodes is quantified according to the fractal nature of the three-phase boundary (TPB). Using this hypothesis an excellent match between modeling and the electrochemical response is found. The origin of the degradation in microstructure and electrochemical performance can be found in the initial fractal roughness of the TPB at a length scale not detectable with state-of-the-art tomography at 30 nm resolution. This additionally implies that the hydrogen electro-oxidation takes place within 4 nm from the geometric TPB line, revealing that the electrochemical reaction zone cannot be regarded anymore as a one-dimensional line when dealing with nanoparticles.

1. Introduction

Solid oxide fuel cells (SOFCs) are highly efficient devices that produce electric energy from the direct electrochemical conversion of a wide range of gaseous fuels, such as hydrogen and methane [1,2]. This technology is expected to play a key role in low-carbon electricity generation due to its capability to flexibly provide electric power with minimal losses, low emissions of pollutants and low levels of noise [3,4].

SOFCs rely on the conduction of oxygen ions, from cathode to anode, through a solid ceramic electrolyte, such as yttria-stabilized zirconia (YSZ) or scandia-stabilized zirconia (ScSZ) [5]. Ion conduction in ceramics occurs at elevated temperatures. For some electrolyte materials and geometries, this results in operating temperatures above 800 °C if internal resistive losses are to be minimized. However, operation at high temperature limits the choice of other materials, in particular sealants and metallic components for the balance-of-plant, and inhibits rapid start-up and shut-down [6]. Therefore, reducing the operating temperature to the range 500–750 °C can pave the way for more cost-effective SOFCs for residential and transport applications [6].

Nonetheless, reducing the operating temperature slows down the thermally-activated charge transfer and charge transport processes occurring at the electrodes and in the electrolyte, thus increasing the polarization and ohmic losses. While ohmic losses can be reduced by producing thinner electrolytes [7,8], the decrease in the charge transfer kinetics can be overcome by replacing conventional cermet electrodes with advanced electrode microstructures, specifically designed to maximize the three-phase boundaries (TPB), which are the sites where electrons, ions and gases electrochemically react. Nanostructured electrodes produced via infiltration meet these requirements [9–12]. Nanostructured electrodes consist of a porous ceramic scaffold, which provides mechanical support and enhanced oxygen ion conduction, whose surface is decorated with metallic nanoparticles deposited through a sequence of infiltration steps, as depicted in Fig. 1a for a Ni-based anode.

While being effective in reducing the polarization resistance, Ni-based infiltrated electrodes undergo fast degradation even at intermediate temperature. Klemensø et al. [13] reported a rapid drop in electronic conductivity and associated tenfold increase in polarization resistance within the first 24 h of operation of Ni-infiltrated/YSZ anodes. Similar results have been shown by Birss and co-workers in several studies [14,15], confirming a dramatic increase in polarization resistance within the first 7 days of operation in the best case scenario.

Generally speaking, the poor stability of Ni-based SOFC electrodes has been attributed to the microstructural evolution of nickel particles,

* Corresponding author.
E-mail address: a.bertei@imperial.ac.uk (A. Bertei).

http://dx.doi.org/10.1016/j.nanoen.2017.06.028
Received 9 May 2017; Received in revised form 14 June 2017; Accepted 15 June 2017
Available online 16 June 2017

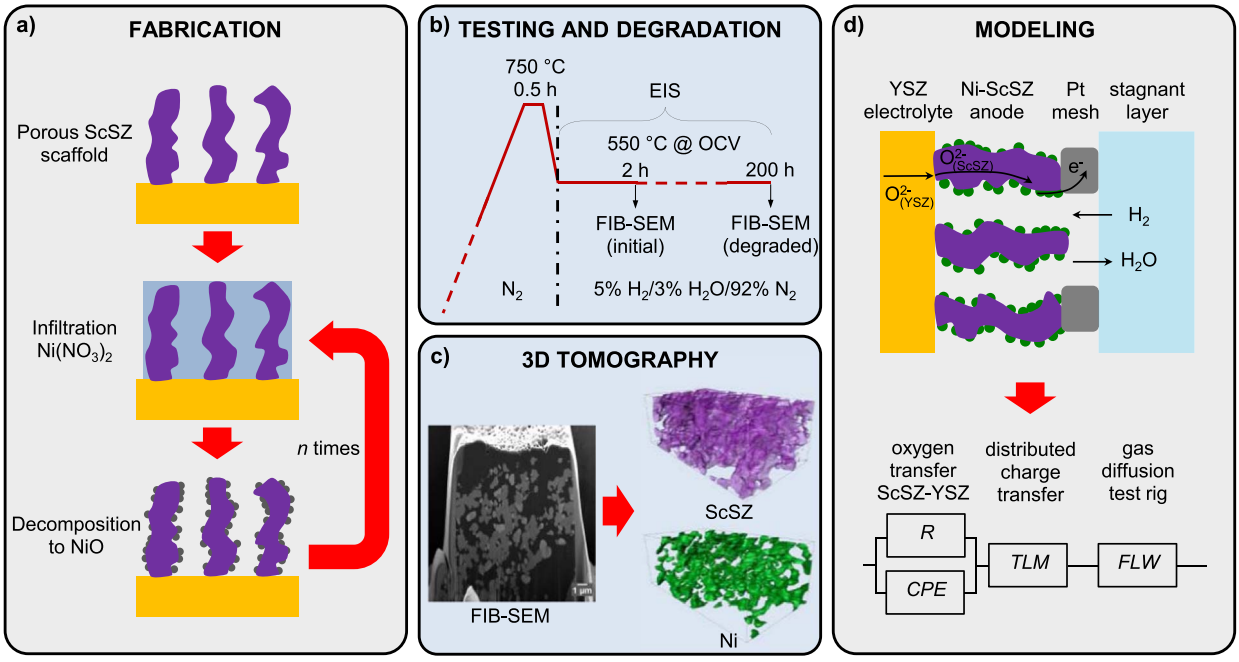

Fig. 1. Schematic flowchart of the methodology used to quantify the electrochemical and microstructural degradation of infiltrated electrodes, comprising a) fabrication of electrodes via infiltration, b) degradation test with real-time measurement of electrochemical impedance, c) *ex-situ* 3D tomographic reconstruction of electrode microstructure, d) modeling of transport and reaction phenomena via a physically-based equivalent circuit.

which tend to coarsen at elevated temperature, thus reducing the connectivity and, ultimately, the active TPB density (length per unit volume) [16,17]. Nickel coarsening has been extensively studied in conventional cermet anodes with the aid of 3D computed tomography, which enables the reconstruction and quantification of the electrode microstructure (see Fig. 1c) [18–20]. Quantitative relationships between the loss in TPB density and the increase in polarization resistance were obtained in conventional cermet electrodes, revealing larger Ni coarsening rates under current and in humidified conditions [17,21–23].

In contrast, the role of the nickel microstructure in the electrochemical degradation of infiltrated electrodes is far less clear. Klemensø et al. [13] claimed that no visible Ni coarsening was observed with SEM for any of the infiltrated anodes showing rapid electrochemical degradation. Similar conclusions were reached by researchers who analyzed microstructures where nickel nanoparticles were produced in-situ, for example as a consequence of redox cycling: the microstructural evolution detected with 3D tomography at 30–50 nm resolution was not sufficient to explain the rapid increase in polarization resistance occurring within the first few hours after each redox cycle preceded by a good performance [24–26].

In this study, for the first time, a comprehensive analysis of the electrochemical and microstructural degradation of Ni-infiltrated anodes is presented by coupling electrochemical impedance spectroscopy (EIS), focused ion beam scanning electron microscopy (FIB-SEM) [27] and physically-based modeling, as depicted in Fig. 1. More specifically, this work focuses on the degradation, at 550 °C under wet hydrogen for up to 200 h, of two pairs of symmetric cells, supported on YSZ electrolyte, fabricated by infiltrating thin ScSZ scaffolds with nickel for 10 times (x10) and 19 times (x19). The combination of these techniques allows for the measurement of the electrochemical degradation in real time via EIS (Fig. 1b) and the *ex-situ* three-dimensional reconstruction and quantification of the microstructural evolution before and after degradation (Fig. 1c). A physically-based equivalent circuit (Fig. 1d), recently presented and validated by the authors in a wide range of electrode microstructures [28], complements the experimental observations and links the microstructural evolution to the degradation of the electrochemical performance, thus enabling the quantification of the different mechanisms that lead to performance loss. The analysis reveals the rough and fractal nature of the TPB, providing an estimate of its effective width, thus giving the resolution requirements for capturing the degradation phenomena that affect nanoparticles in infiltrated electrodes.

2. Materials and methods

2.1. Electrode manufacturing and testing

ScSZ was selected as scaffold material due to its chemical stability and high ionic conductivity at intermediate temperatures [5,29]. Symmetrical cells of ScSZ $(Sc_2O_3)_{0.10}(ZrO_2)_{0.90}$ scaffolds on top of a dense YSZ electrolyte were produced as follows. A slurry was prepared in-house by using ScSZ (Fuel Cell Materials, 8.9 $m^2\ g^{-1}$) and carbon black as pore former (Alfa Aesar, 75 $m^2\ g^{-1}$), suspended in terpineol, Hyperdermer (KD15) as dispersant and an ethylcellulose binder (Hercules ECN-7). The slurry was tape cast on both sides of the YSZ support (250 µm, Fuel Cell Materials) and sintered at 1250 °C for 2 h, resulting in an 8–10 µm-thick porous layer after sintering.

The sintered ScSZ scaffolds were impregnated at room temperature on both sides with a 2 M ethanol solution of $Ni(NO_3)_2$ (Aldrich). Very small aliquots of solution were used to avoid accumulation of nickel at the top of the scaffold and spillages that may have short-circuited the cell. After each infiltration the samples were fired at 550 °C to decompose the nitrate to NiO [30]. This procedure was repeated ten times for one pair of samples (samples x10) and nineteen times for a second pair of samples (samples x19). Weight changes were used to determine the mass of the ScSZ scaffold and of the infiltrated nickel.

To measure impedance, all the symmetrical cells were put in an in-house built apparatus [31] and fired in N_2 at a rate of 5 °C min^{-1} up to 750 °C for 30 min, then cooled at a rate of 10 °C min^{-1} down to 550 °C to reduce NiO to Ni metal in a 5% H_2/3% H_2O atmosphere. After the introduction of hydrogen, the electrochemical impedance was measured at selected intervals at open-circuit conditions, under 5% H_2/3% H_2O atmosphere, for up to 200 h. The EIS response was collected with a potentiostat (Autolab PGSTAT302) in the frequency range 10^{-1}–10^6 Hz with an AC potential of 20 mV, using platinum mesh as a current collector.

2.2. 3D characterization

The microstructure of infiltrated anodes was reconstructed before and after degradation at 550 °C. In this study, the microstructure after 2 h from reduction was referred as the nominal initial microstructure (see Fig. 1b).

Both initial and degraded anodes were impregnated with epoxy resin (Struers, UK) under low vacuum before being cross-sectioned and coated in gold in preparation for focused ion beam milling [27]. A Ga-ion beam was used to mill regions of ca. 10 × 10 × 10 µm using a current of 1 nA. Consecutive images were acquired every 30 nm under a 1.5 kV accelerating voltage and an average pixel size of 24.5 nm on a ZEISS Auriga FIB-SEM setup. Each acquisition varied slightly in terms of volume acquired and pixel size as reported in Table S1. Density contrast enabled the identification of the pore phase (black), the ScSZ scaffold (dark gray) and the Ni phase (bright) on the exposed surface.

SEM images were processed using open source and commercial software such as ImageJ [32], Avizo 7.0.1 (Visualization Science Group, Mérignac, France) and Matlab R2015b (The Mathworks Inc., MA, USA). Images were cropped and aligned using a least square fit to account for drift in the xy direction before being sheared-corrected. Grayscale datasets were smoothed using a 3 × 3 × 3 median filter and an edge-preserving smoothing filter modeled on a non-linear diffusion process. Datasets were then segmented using a threshold-dependent region-growing algorithm with manually determined seeds [33]. All phases were filtered by volume to remove voxel-sized artifacts.

The segmentation of the three phases allowed for the calculation of phase percentages and the quantification of microstructural metrics for each individual phase. The open source Matlab application TauFactor [34] was used to evaluate percolation, surface area and tortuosity factor of each phase as well as the TPB density. The mean intercept length [35] of each phase was calculated for all the voxels along the three orthogonal directions by weighting on volumetric basis. Separation of each phase into individual agglomerates, necessary to study morphological changes with a higher level of sophistication, was done by using a binary watershed algorithm implemented in Quiq3D (IQM Elements, London, UK) [36]. The individual Ni agglomerates were filtered by volume to remove voxel-sized artifacts by using a cut-off volume with a radius of 75 nm. This advanced quantification allowed for the evaluation of the agglomerate size distribution and the sphericity, which is the ratio between the surface area of a sphere with equivalent volume and the surface area of the agglomerate [37]. Simpleware ScanIP 7.0 (Synopsys, Mountain View, USA) was used for resampling the microstructures for the calculation of the fractal dimension according to the "majority wins" interpolation [38]. A synthetic microstructure, generated according to the packing algorithm described by Bertei et al. [39], was considered as a reference case for non-fractal TPB. The cellular automaton developed by Wang and Atkinson [40–42], based on the free energy minimization by using an interface imbalanced interaction model and taking into account both evaporation/condensation and grain growth mechanisms, was used to reproduce the roughness evolution. All calculations (volumes, TPB, intercept lengths, surface and interfacial areas) were based on voxel-counting methods.

2.3. Electrochemical modeling

The deconvolution of the impedance spectra and the estimation of the TPB density from the resistance associated to the distributed charge transfer were performed according to a physically-based one-dimensional model previously validated by the authors [28], which is schematized in the equivalent circuit in Fig. 1d. The model takes into account three different contributions: i) the oxygen transfer between ScSZ and YSZ at the electrode-electrolyte interface, represented by a parallel combination of resistance and constant phase element (CPE), ii) the distributed charge transfer along the electrode thickness, represented by a transmission line model (TLM), and iii) the multi-component gas diffusion in the test rig, represented by a finite-length Warburg element (FLW). Only the TLM is described in the following because, as shown later in Section 3.1, the electrochemical degradation affects only the medium-frequency impedance feature, which is associated to this circuit element.

The TLM describes the ionic ohmic transport and the charge transfer reaction at the TPB distributed along the anode thickness. Electronic ohmic losses and gas concentration resistance within the anode thickness were proved to be negligible due to the small electrode thickness and the high Ni conductivity and H_2 diffusivity [28]. Assuming uniform microstructural properties, the area-specific resistance R_{TLM} associated to the charge transfer at the distributed TPB results as follows [28]:

$$R_{TLM} = 2\frac{t_{an}}{k_{eff}\sigma_{io}(1-f_c)}\frac{\coth(\Gamma)}{\Gamma} \text{ with } \Gamma = t_{an}\sqrt{\frac{F}{RT}\frac{i_0 L_{TPB}}{k_{eff}\sigma_{io}}} \quad (1)$$

where t_{an} is the anode thickness, f_c the fraction of electrode area covered by the Pt mesh (which is inaccessible to gas), F the Faraday constant, R the gas constant, T the absolute temperature while the factor 2 takes into account that there are two electrodes per symmetric cell. The exchange current density per unit of TPB length i_0 and the bulk ionic conductivity of ScSZ σ_{io}, estimated as reported in a previous study of the authors [28], are regarded as microstructural-independent parameters. On the other hand, the TPB density per unit of electrode volume L_{TPB} and the effective conductivity factor k_{eff} of the ScSZ phase [43] depend on the electrode microstructure. In particular, by fixing all the other parameters, L_{TPB} can be evaluated by using Eq. (1) from the medium-frequency resistance R_{TLM} measured with EIS. When the roughness factor χ is considered in the model, the product $\chi \cdot L_{TPB}$ is substituted for L_{TPB} in Eq. (1).

3. Results and discussion

3.1. Electrochemical degradation

The electrochemical degradation of the anodes was measured using real-time impedance spectroscopy in symmetric cells at 550 °C under 5% H_2/3% H_2O at open-circuit voltage (OCV). These operating conditions are relevant for low-temperature operation and allow for the detection of changes of impedance in a reasonable time scale. Fig. 2 shows the results obtained for the anode infiltrated 19 times with nickel (sample x19) as a function of time. This sample was chosen as a benchmark because it has a sufficient nickel volume fraction to avoid percolation losses. The impedance spectra in Fig. 2a show four features: i) an ohmic resistance, attributed to the YSZ electrolyte, ii) a high-frequency small feature, due to the oxygen transfer resistance between ScSZ and YSZ, iii) a medium-frequency depressed feature, attributed to the charge transfer distributed at the TPB along the electrode thickness, and iv) a low-frequency semicircle, associated to the gas diffusion in the test rig. The characteristic frequencies of the processes are reported in Fig. S1. The electrochemical model, validated previously by the authors [28], provides the basis for the deconvolution of the different impedance features and their attribution to different electrochemical processes.

Fig. 2a shows that only the medium-frequency feature increases over time. This is consistent with reports by other authors for Ni-infiltrated YSZ scaffolds [13–15]. The temporal evolution of the four resistances is summarized in Fig. 2b. The resistance of the medium-frequency process associated to the distributed charge transfer at the TPB increases significantly within the first 2 h, then keeps increasing at a smaller rate for the next 100 h, followed by stabilization for the last 100 h. This indicates an evolution of the electrode microstructure, which is quantified in the next Section. On the other hand, the ohmic, oxygen transfer and gas diffusion resistances remain fairly constant with time, implying no electrochemical degradation of the YSZ

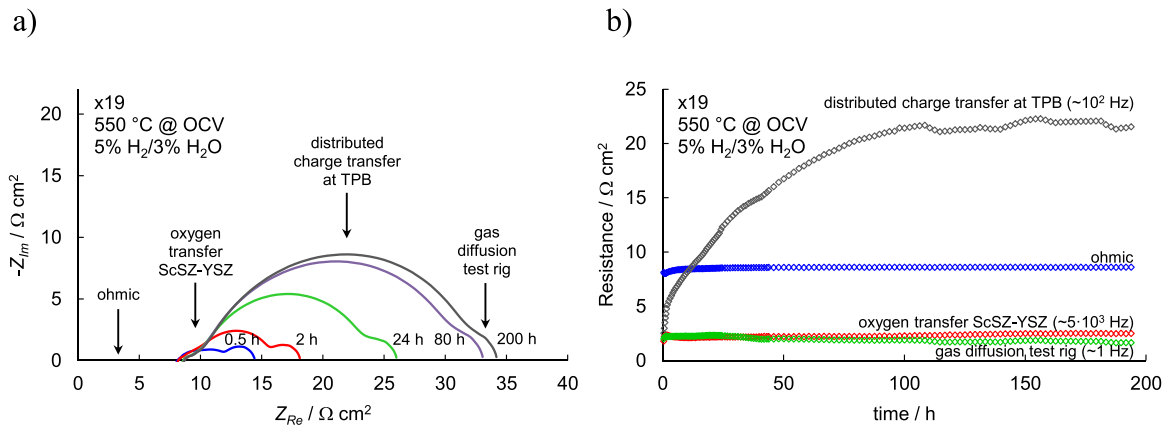

Fig. 2. Electrochemical degradation of anode x19 tested at 550 °C, OCV, 5% H_2/3% H_2O: a) impedance spectra at different times, b) deconvolution of the resistances as a function of time.

electrolyte, the ScSZ/YSZ interface nor of the stagnant diffusion layer in the test rig.

3.2. Quantification of the microstructural evolution

The 3D reconstruction of the electrode microstructure before and after degradation was performed using FIB-SEM tomography with an average voxel size of ca. 30 nm. Such a voxel size represents the state-of-the-art of 3D tomographic reconstruction of SOFC electrodes, typically considered the tradeoff between the minimum spatial resolution required to distinguish meaningful microstructural features while attaining a sufficient field of view to reconstruct a volume big enough to be statistically representative [44–47]. Further details regarding the imaging conditions and volumes analyzed are reported in Table S1. Fig. 3 shows a visual representation of a grayscale slice and the reconstructed 3D microstructure for the x19 anode before and after degradation. The ScSZ scaffold (gray in the xy slice, purple in the 3D visualization) provides a continuous network throughout the volume of the sample, while the nickel phase (bright in the xy slice, green in the 3D visualization) is dispersed on the surface of the ScSZ scaffold, as expected in an electrode prepared by wet infiltration [9–11]. While the ScSZ scaffold remains fairly unchanged upon degradation, Fig. 3 shows that nickel is present in bigger agglomerates in the degraded sample. As a consequence of this structural reorganization of nickel, there is less connected three-phase boundary in the degraded anode than in the initial one, as clearly visible in Fig. 3.

Quantitative information of the microstructural evolution is reported in Fig. 4. The contact area between Ni and ScSZ decreases after degradation in both x10 and x19 anodes (Fig. 4a), indicating that nickel tends to de-wet the scaffold. Similarly, there is a decrease in Ni-pore contact area after degradation, which exposes the ScSZ scaffold to the pore phase, as reported in Fig. S3. In particular, Ni phase grows during the annealing (Fig. 4c and e) and Ni agglomerates tend to become rounder (Fig. 4f). The tortuosity factor of the whole Ni phase increases after degradation (Fig. 4b), especially for lower nickel content as in the x10 anode, which is an indication of loss in Ni connectivity. On the other hand, the ScSZ ceramic scaffold does not show any significant evidence of microstructural evolution as reported in Fig. S4, because the mobility of ScSZ is negligible at 550 °C after being sintered at 1250 °C [48,49]. Ultimately, the TPB density decreases in both x10 and x19 anodes after degradation, as reported in Fig. 4d. Notably, the TPB density of the initial samples are in quantitative agreement with the

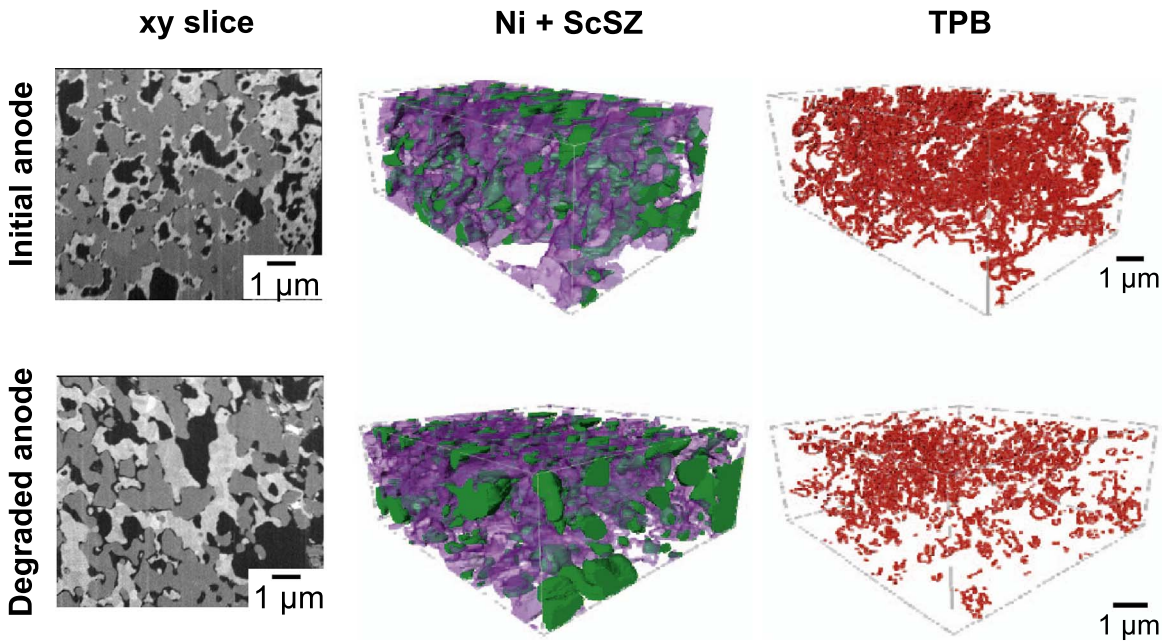

Fig. 3. FIB-SEM reconstruction of anode x19, from grayscale slices (left), to 3D segmented volumes (middle) and identification of percolating three-phase boundaries (right) for both the samples before degradation (top) and after degradation (bottom). In the SEM slices, Ni is the bright phase, ScSZ the gray phase and pores are black; in the 3D reconstruction, Ni is reported in green, ScSZ in purple, pores are transparent while percolating three-phase boundaries are in red. A 3D rendering without surface smoothing is reported in Fig. S2.

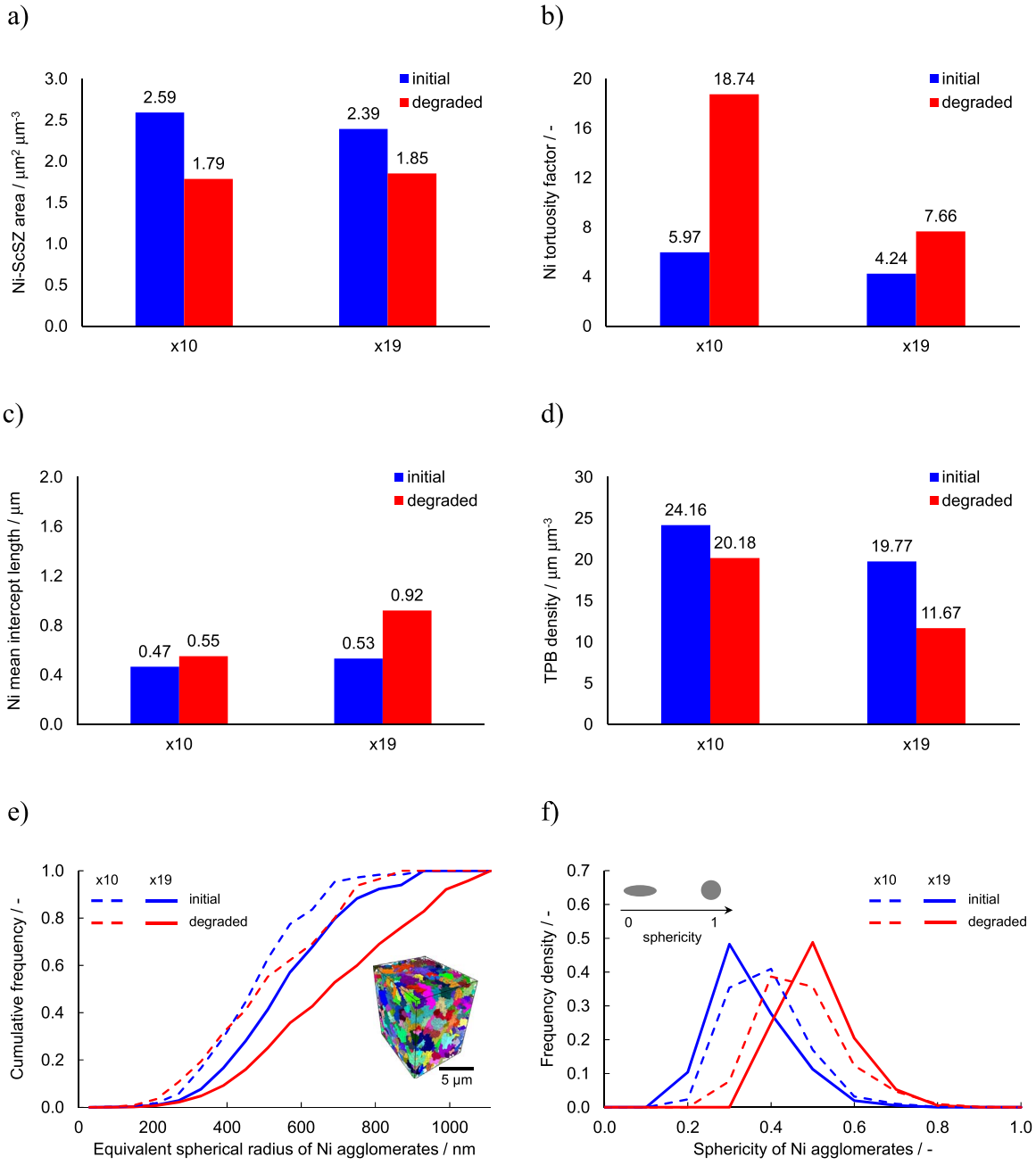

Fig. 4. Quantification of microstructural properties of the anodes x10 and x19 before and after degradation: a) Ni-ScSZ contact area per unit of electrode volume, b) tortuosity factor of Ni phase, c) volume-averaged mean intercept length of Ni phase, d) active TPB density per unit of electrode volume, e) cumulative frequency distribution of the equivalent spherical radius of Ni agglomerates (shown in the inset), f) frequency density distribution of sphericity of Ni agglomerates.

values reported by the 3D reconstruction of infiltrated anodes [27].

Hence, the quantification of the electrode microstructure before and after degradation of Ni-infiltrated anodes with two nickel loadings shows indications of a microstructural evolution compatible with the coarsening of Ni phase, qualitatively similar to conventional cermet Ni-based anodes [17,21–23,50].

3.3. Linking microstructural and electrochemical degradation via modeling

The relationship between the electrochemical degradation shown in Section 3.1 and the microstructural evolution presented in Section 3.2 is investigated here by means of a physically-based electrochemical model [28]. By using Eq. (1) the model can infer the temporal evolution of the TPB density from the time-dependence of the medium-frequency resistance measured with impedance spectroscopy as in Fig. 2b. A similar approach has already been applied successfully in annealed conventional cermet electrodes [23] and attempted in Ni-$La_{1-x}Sr_xGa_{0.8}Mg_{0.2}O_{3-\delta}$ infiltrated electrodes [51], although without real-time EIS data and 3D tomographic reconstruction.

Fig. 5 shows the TPB density estimated from EIS data by using the electrochemical model, assuming all the electrochemical degradation is caused by a decrease in TPB density. The parameters used in the simulation, assumed constant with time, are reported in Table S2. In order to reproduce the rapid increase in charge transfer resistance reported in Fig. 2b, the model predicts a fast decrease in TPB density, especially within the first 50 h, followed by stabilization. The comparison with the TPB density evaluated before and after degradation with FIB-SEM tomography (symbols) shows a discrepancy between the 3D tomographic reconstruction and the model prediction. The discrepancy

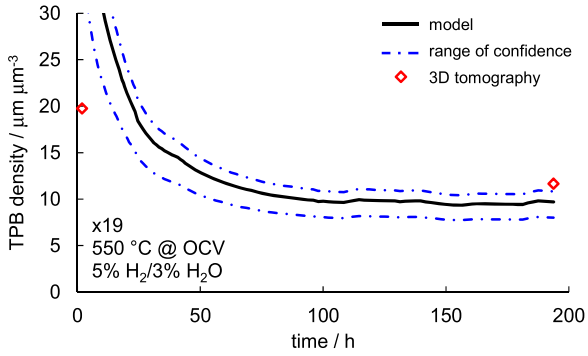

Fig. 5. Estimation of TPB density as a function of time from EIS data according to the electrochemical model (solid line) in comparison with data obtained with FIB-SEM tomography (symbols). The dot-dashed lines refer to the range of confidence of model prediction according to the sensitivity to uncertain parameters. Results refer to the anode x19 tested at 550 °C, OCV, 5% H_2/3% H_2O.

is not caused by inaccurate EIS data, since they are consistent with the literature [13–15] as discussed above, and cannot be attributed to an incorrect evaluation of model parameters: even by taking into account the variability of uncertain parameters used in the simulation (see Table S2), the experimental TPB densities evaluated with FIB-SEM tomography fall outside the range of confidence predicted by the model (see dot-dashed lines in Fig. 5). In particular, the TPB density predicted by the model in the first few hours (> 30 μm μm^{-3}) is too high if compared with the value measured with FIB-SEM tomography in the initial sample (19.77 μm μm^{-3}).

The model indicates that there is more electrochemical degradation than expected from the microstructural evolution analyzed in Section 3.2. The charge transfer resistance should scale inversely with the TPB density in the worst case scenario (i.e., Γ « 1, see Eq. (1)). On the contrary, while the TPB density of the x19 anode decreases by 41% after degradation (Fig. 4d), the resistance associated to charge transfer increases from 5.3 Ω cm^2 after 2 h to 21.5 Ω cm^2 after 200 h, that is, more than 4 times. This means that the electrochemical degradation measured with impedance spectroscopy cannot be solely attributed to the microstructural evolution identified with FIB-SEM tomography at the given resolution.

3.4. Roughness of the three-phase boundary

3.4.1. The roughness hypothesis

The mismatch between the TPB density predicted according to the electrochemical degradation and the 3D characterization before and after degradation requires careful analysis.

The literature reports several evidences of rapid electrochemical degradation without significant microstructural evolution when dealing with Ni nanoparticles. Possible explanations stem from the poisoning of the TPB by SiO_2 deposition, which is preventable by avoiding Si-based glass [52,53], or by impurities present in the raw materials [53]. However, these two hypotheses are set aside considering that similar degradation trends in Ni-infiltrated anodes have been reported by different groups working with different equipment, testing procedures and infiltration routes (e.g., molten salts, ethanol or aqueous solution, with or without vacuum assistance) [13–15]. Therefore, another explanation, closely related to the intrinsic nature of the TPB when dealing with nanoparticles, must be considered.

Klemensø et al. reported a rapid degradation in polarization resistance of Ni-infiltrated YSZ scaffolds without any visible change in microstructure according to their observations [13]. Similar results were reported in conventional Ni-YSZ cermet anodes after experiencing redox cycles. In such a case, the oxidation to NiO is associated to volume expansion [54] so that, after subsequent reduction to Ni metal, nickel nanoparticles are generated in-situ at the interfaces [53], causing an initial increase in the electrochemical performance due to the enhanced TPB density [24]. After a few hours of annealing, there is a rapid increase in polarization resistance which cannot be explained by the evolution of the TPB, which does not decrease as rapidly [25].

An alternative explanation for the mismatch reported above stems from the consideration that FIB-SEM tomography may not be able to capture the fine microstructural changes taking place at a length scale smaller than the resolution used in 3D tomography, which is in the order of 30 nm. Fig. 6a and b compare a representative cross section of the x19 initial anode as imaged with field emission gun-SEM (FEG-SEM) and FIB-SEM. The images, although representative of tens of similar regions, refer to different selections because both FEG-SEM and FIB-SEM involve destructive imaging procedures. The FEG-SEM image in Fig. 6a, taken at a higher level of magnification, shows a fine texture of Ni nanoparticles deposited on the top of a ScSZ particle. These Ni nanoparticles are connected with each other and have sufficient inter-particle porosity to allow gases to reach the three-phase boundaries. On the other hand, the fine texture is not detectable by using state-of-the-art FIB-SEM tomography (Fig. 6b), whose resolution of 30 nm is not sufficient to resolve these small microstructural details. A heuristic viewpoint on the nature of the TPB in Ni-infiltrated anodes is sketched in Fig. 6c: the real, rough nature of the Ni-ScSZ interface and so of the three-phase boundary is effectively smoothed due to the finite resolution of FIB-SEM tomography and associated image processing. This is the famous coast-line paradox made popular by Benoit Mandelbrot [55]: the more one zooms in into a rough structure (such as the TPB), the more details appear. The hypothesis made in this study, which is corroborated at the end of this Section, is that the

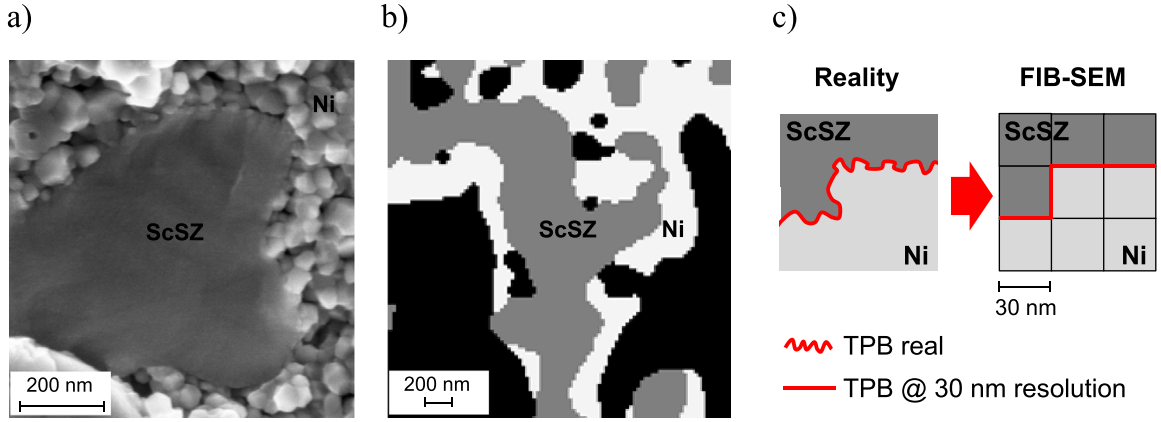

Fig. 6. Roughness of the TPB before degradation: a) FEG-SEM image, b) xy slice as obtained from FIB-SEM after segmentation, c) schematic representation of the smoothing of the TPB length as a consequence of the finite resolution of FIB-SEM tomography. Images refer to the anode x19 before degradation.

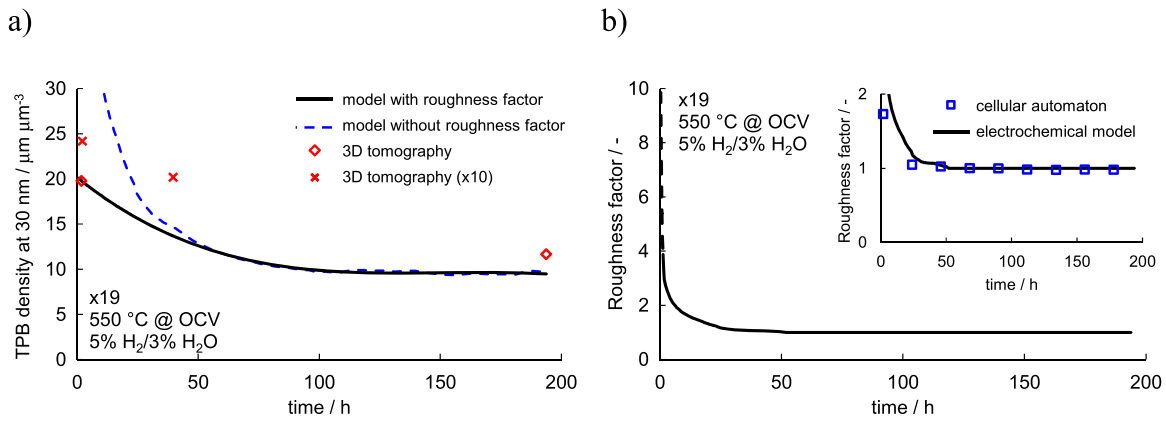

Fig. 7. Estimation of TPB density from EIS data when using the roughness factor in the model: a) TPB density at 30 nm resolution (the dashed blue line refers to the results reported in Fig. 5), and b) roughness factor as a function of time. In a), results from FIB-SEM tomography of anode x10 (crosses) are reported to highlight the same trend of TPB density at 30 nm resolution predicted by the model with roughness factor (black). In b), the inset reports the ratio of TPB density with and without 7.5% of nanopores in the Ni phase by using a cellular automaton (symbols). Results refer to the anode x19 tested at 550 °C, OCV, 5% H_2/3% H_2O.

microstructural details detectable with FIB-SEM tomography at 30 nm resolution are not sufficient to capture the real TPB length in as-reduced Ni-infiltrated electrodes, which ultimately is responsible for the majority of the electrochemical degradation of the electrode.

In order to reproduce this phenomenon, a roughness factor χ is introduced in the electrochemical model: the roughness factor represents the length of real TPB (L_{TPB}^{real}) per unit length of TPB resolved at the FIB-SEM resolution of ca. 30 nm (L_{TPB}), that is, $\chi = (L_{TPB}^{real})/L_{TPB}$. Therefore, the real TPB density is calculated according to the product $\chi \cdot L_{TPB}$. As reported in Fig. S5, the sharp decrease in the medium-frequency electrode capacitance over time indicates that the roughness factor χ approaches 1 after 50 h of degradation. This information allows for the co-fitting of both the TPB density and the roughness factor from the EIS data in Fig. 2b according to the electrochemical model. Results are reported in Fig. 7. The TPB density at 30 nm resolution is estimated within the range 50–200 h (i.e., where $\chi = 1$) from the time-dependence of the distributed charge transfer resistance reported in Fig. 2b, exactly as performed before in Fig. 5. Such a trend is extrapolated backwards within the first 50 h, resulting in the black solid line in Fig. 7a, which represents the TPB density at 30 nm resolution estimated with the electrochemical model from EIS data. The ratio between the TPB density estimated previously without roughness factor (blue dashed line in Fig. 7a) and the TPB density extrapolated at 30 nm resolution (black solid line in Fig. 7a) equals the roughness factor χ, which is reported in Fig. 7b. Fig. 7b also reports the ratio between the TPB density with and without 7.5% vol. of nanopores, as small as 30 nm, randomly dispersed within the nickel phase, as predicted by a cellular automaton [40–42]. The size and volume fraction of nanopores were chosen according to the visual inspection of Fig. 6a and the analysis of Ni volume change after degradation. Considering nanopores within the nickel phase represents a simple, preliminary way to quantitatively reproduce the roughness factor according to the comparison between Fig. 6a and b. The cellular automaton simulates the microstructural evolution of the Ni phase according to different coarsening mechanisms, such as evaporation-condensation and slow grain growth, thus providing an alternative approach to reproduce the microstructural evolution independently from impedance spectroscopy and the electrochemical model.

Several observations can be derived from the analysis of Fig. 7:

1. the TPB density at ca. 30 nm resolution estimated using the roughness factor (black solid line) is in fair agreement with the TPB density evaluated before and after degradation with FIB-SEM tomography (diamonds): there is no longer any significant mismatch between model predictions and experimental observations. Notably, the predicted trend is corroborated by the intermediate data points provided by the tomographic results of sample x10 (crosses);
2. the TPB density at 30 nm resolution decreases with time more smoothly than in Fig. 5, being in qualitative agreement with the predictions obtained with phase field modeling approaches [56,57]. On the other hand, L_{TPB} does not follow the power law $L_{TPB} \propto (l_0^n + k_D \cdot t)^{-2}$ suggested by Miller et al. [51], where l_0 is the Ni particle size at time zero and k_D is the Ni surface diffusion coefficient, which is indeed expected to hold only for long-term annealing at temperatures higher than those used in this study [23,58];
3. the roughness factor decreases much more rapidly than the TPB density at 30 nm resolution, being smaller than 1.2 after 24 h of degradation at 550 °C (Fig. 7b). Such a faster trend is reasonable because the roughness factor represents the microstructural evolution of nanometric features at the TPB, which are expected to coarsen more rapidly than the microstructure at the µm-length scale;
4. the results of the cellular automaton (Fig. 7b, symbols) are in fair agreement with the roughness factor evaluated by the electrochemical model (solid line), supporting the hypothesis of a rapid evolution of the nanometric microstructural features at the TPB.

3.4.2. Validation of the roughness hypothesis: the fractal dimension of the TPB

The introduction of the roughness factor allows for a coherent explanation of the degradation trends in Ni-infiltrated anodes, complementing the analysis made with FIB-SEM tomography. It only remains to estimate how small the features generating the TPB roughness are. This is performed by calculating, for the first time ever according to authors' best knowledge, the fractal dimension of the three-phase boundary, as reported in Fig. 8. The initial microstructures of anodes x10 and x19 are resampled by using larger voxels as reported in Fig. 8a. In the context of 3D tomography, this resampling process reproduces the imaging of the microstructure with a coarser resolution [38], where the average voxel size r is calculated according to the geometric mean of the voxel length in the three directions. By plotting the TPB density at different resolutions in a log-log plot, the fractal dimension D of the TPB is calculated from the slope of the straight lines in Fig. 8b according to the Mandelbrot formula [55]:

$$L_{TPB} = M \cdot r^{1-D} \rightarrow Log(L_{TPB}) = m + (1 - D) \cdot Log(r) \quad (2)$$

where M is a positive scaling factor. Fig. 8b shows that there is a clear correlation of the TPB density as a function of resolution for the initial microstructures x10 and x19, resulting in a fractal dimension which is approximately equal to 1.5 within 3.5% of deviation for both the initial samples, meaning that the TPB cannot be viewed as a line. Notably, upon resampling, a synthetic microstructure of spherical particles

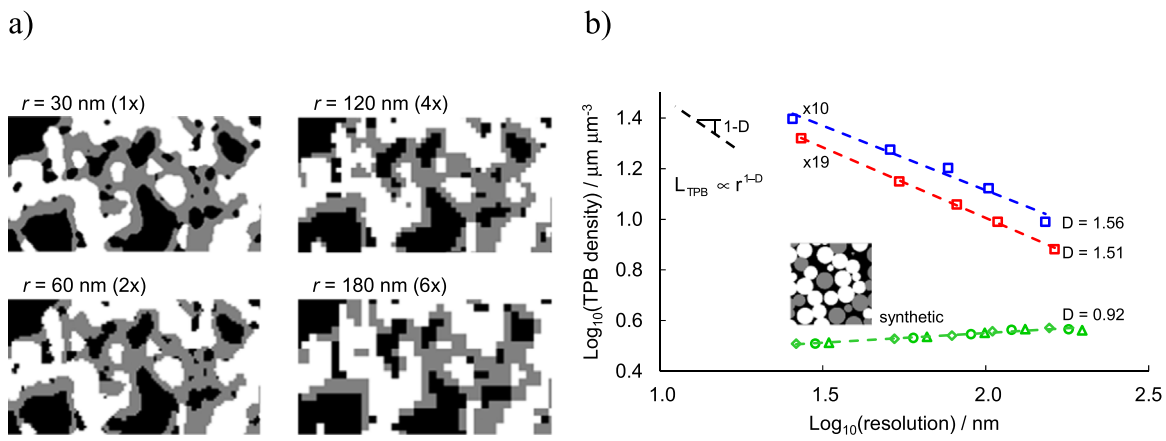

Fig. 8. Effect of the resolution on TPB density evaluation from 3D tomography: a) resampling of the microstructure with larger voxel size, b) log-log plot of the TPB density as a function of the resolution and evaluation of the fractal dimension *D*. The results for the synthetic structure (green) refer to both originally isotropic voxels (30–30–30 nm, circles) and non-isotropic voxels (30–30–20 nm, diamonds; 30–30–40 nm, triangles).

correctly shows a fractal dimension of ca. 1, since the TPB is not rough in such a case. In addition, the excellent alignment of synthetic data in Fig. 8b (green symbols) regardless the voxel isotropy suggests that the TPB fractal dimension is not affected by voxel anisotropy. Therefore, the straight lines in Fig. 8b for initial structures x10 and x19 reveal that the smaller the voxel size *r*, the larger the TPB density that one would measure with a tomographic apparatus capable of resolving smaller and smaller features, as also confirmed by recent tomographic studies [59]. The effect of resolution on the evaluation of microstructural properties from 3D tomography has already been introduced in the fuel cell community [38,44,59], but not in this perspective and without attempting to calculate the fractal dimension.

The dependence of the TPB density from tomographic resolution in Fig. 8b reveals the rough, fractal nature of the TPB in Ni-infiltrated electrodes. However, as every fractal in nature, the fractal dimension remains constant down to a cut-off resolution, beyond which the roughness disappears and is not relevant anymore. The cut-off resolution is estimated by using the roughness factor χ evaluated from EIS data in Fig. 7b. In particular, for the anode x19, the roughness factor after 2 h (i.e., the nominal initial conditions) is equal to 2.95, which corresponds to the ratio between the TPB density at the cut-off resolution and the TPB density at the given tomographic resolution. By considering the fractal dimension D = 1.56 and the resolution used to image the initial microstructure r = 27.2 nm, Eq. (2) can be rearranged to evaluate the cut-off resolution as $r_{cut\text{-}off} = r \cdot \chi^{1/(1-D)}$ = 4 nm. Notably, 4 nm corresponds to about 11 atomic layers in a Ni crystal.

This calculation indicates that below 4 nm the fractal roughness of the TPB is not relevant anymore from an electrochemical point of view. In fact, such a cut-off length comes from the extrapolation of the fractal nature of the TPB down to the resolution relevant for the electrochemistry, as the roughness factor χ is extrapolated directly from the electrochemical degradation measured with impedance spectroscopy in Fig. 2. The cut-off length of 4 nm estimated in this study compares fairly well with the lateral extension of the TPB, equal to 5 nm, predicted by mechanistic modeling studies focusing on the elementary kinetics of hydrogen oxidation. In particular, both Goodwin et al. [60] and Vogler et al. [61] predicted that the adsorption of gas species, their surface diffusion towards the TPB and the hydrogen spillover take place within 5 nm from the geometric TPB line. In other words, the reaction zone must be regarded as an extended three-phase boundary region of ca. 4–5 nm. Notably, due to the exponential dependence in Eq. (2), an error of ± 20% in the evaluation of D would have resulted in a significant deviation in the estimation of the TPB lateral extension as large as ± 95%. This high sensitivity, along with the good match with the predictions of kinetic models and the narrow deviation of D in two samples, heuristically support the robustness of the calculation of the TPB fractal dimension.

For the first time, by analyzing the electrochemical and microstructural degradation of Ni-infiltrated electrodes, an independent verification of the extension of the TPB is provided. Such a quantitative agreement with the TPB extension predicted by mechanistic elementary models provides a fair indication about the soundness of the analysis reported in this Section concerning the fractal roughness of the TPB, which is not captured by FIB-SEM tomography, while being responsible for the fast electrochemical degradation.

3.5. Practical implications of the three-phase boundary fractal roughness

Taking into account the rough, fractal nature of the three-phase boundary in Ni-infiltrated anodes before degradation explains the previously reported mismatch between the electrochemical degradation measured with EIS and the microstructural evolution quantified with FIB-SEM tomography. This analysis generates important implications which go beyond the extent of the present study:

1. the hydrogen oxidation reaction takes place within a width that extends for at least 4 nm from the geometrical three-phase boundary line. Such an extension can be neglected and the TPB can be regarded as a geometric one-dimensional line provided that the size of the characteristic microstructural features is at least an order of magnitude larger than 4 nm, such as in conventional Ni-YSZ anodes as well as in aged or pre-annealed electrodes [23,62]. On the contrary, when dealing with Ni nanoparticles, the nanometric features related to the TPB roughness evolve within the first few hours of degradation, so the TPB extension must be taken into account during this period of time;
2. the minimum resolution required to resolve the TPB roughness in Ni-infiltrated electrodes is in the order of 4 nm. Shimura et al. [44] were able to reconstruct SOFC anodes with a voxel size of 3 nm, but filters should be used to attenuate the fluctuations due to the drift in each image acquisition, resulting in an effective resolution of 15 nm. Therefore, every 3D reconstruction of non-degraded nanostructured electrodes must consider the limits of image resolution and correct for the proper roughness factor taking into account the fractal nature of the TPB. This is particularly relevant when extracting intrinsic kinetic parameters, such as the exchange current density, from EIS data by using the TPB density evaluated with 3D tomography;
3. as evident by comparing Figs. 7a and 2b, most of the electrochemical degradation in Ni-infiltrated electrodes is due to the evolution of the TPB nanometric roughness. Co-infiltrating sintering inhibitors as big

as > 50 nm can be effective to constrain the coarsening of Ni nanoparticles and prevent loss in electronic conductivity [13], whereas such an approach is expected to be ineffective to stop the evolution of the nanometric fractal roughness causing the loss in effective TPB length, which takes place at a smaller length scale. The rapid evolution of the TPB roughness can be potentially attenuated by controlling the interfacial energy among Ni grains and the wetting properties between Ni and the ceramic scaffold material [40,57].

4. Conclusions

For the first time the degradation of SOFC nanostructured anodes, prepared by infiltration of ScSZ scaffolds with nickel (20–30% vol.), was addressed by combining real-time impedance spectroscopy, *ex-situ* 3D tomography and physically-based modeling. By operating the anodes at 550 °C at open-circuit under wet hydrogen, a rapid increase in the medium-frequency charge transfer resistance was revealed after a few hours of operation, with stabilization after 100 h. The quantification of the three-dimensional microstructure reconstructed at ca. 30 nm resolution with FIB-SEM tomography revealed a decrease in active TPB density compatible with Ni coarsening. However, according to the electrochemical model, such a microstructural evolution was not sufficient to explain the significant increase in charge transfer resistance. A roughness factor, equal to the effective TPB length per unit of TPB detectable at 30 nm resolution, was introduced to explain the mismatch. Such a roughness factor was corroborated by two independent approaches, that is, a simulation with a cellular automaton and by the calculation of the fractal dimension of the TPB, estimating an extension of the TPB width in the order of 4 nm, compatible with the predictions of elementary kinetic models.

The study revealed that most of the initial electrochemical degradation in Ni-based nanostructured anodes comes from the evolution of the TPB at the nanoscale, thus posing serious limitations to imaging techniques and providing the minimum resolution requirements for following the degradation. Similar conclusions are shared for electrodes in which Ni nanoparticles are generated in-situ, for example as a result of redox cycles. This suggests that the rapid electrochemical degradation of nanostructured anodes can be attenuated by modifying the interfacial energy among Ni grains and between Ni and the ceramic scaffold rather than co-infiltrating sintering inhibitors, which are ineffective at such a nanometric length scale. In addition, the quantification of the rough, fractal nature of the three-phase boundary, the cut-off length and its impact on the electrochemistry provide the basis for re-thinking the role of the interfaces in nanostructured electrodes, overcoming the current paradigms used in the fuel cell community.

Acknowledgements

This project has received funding from the European Union's Horizon 2020 research and innovation programme under the Marie Skłodowska-Curie grant agreement No 654915 and the EPSRC grant EP/M014045/1. IQM Elements (London) is acknowledged for the use of Quiq3D software and 3Blue1Brown for mathematical inspiration. Helpful discussions with Dr. Paul Boldrin and Dr. Samuel J. Cooper (Imperial College London) are gratefully acknowledged. Data underpinning this publication is available at: https://doi.org/10.5281/zenodo.810090.

Appendix A. Supporting information

Supplementary data associated with this article can be found in the online version at doi:10.1016/j.nanoen.2017.06.028.

References

[1] S.C. Singhal, K. Kendall, High Temperature Solid Oxide Fuel Cells: Fundamentals, Design And Applications, Elsevier, Oxford, 2003.
[2] Y. Choi, E.C. Brown, S.M. Haile, W.C. Jung, Electrochemically modified, robust solid oxide fuel cell anode for direct-hydrocarbon utilization, Nano Energy 23 (2016) 161–171.
[3] P.P. Edwards, V.L. Kuznetsov, W.I.F. David, N.P. Brandon, Hydrogen and fuel cells: towards a sustainable energy future, Energy Policy 36 (2008) 4356–4362.
[4] S.C. Singhal, Advances in solid oxide fuel cell technology, Solid State Ion. 135 (2000) 305–313.
[5] A.J. Jacobson, Materials for solid oxide fuel cells, Chem. Mater. 22 (2010) 660–674.
[6] D.J.L. Brett, A. Atkinson, N.P. Brandon, S.J. Skinner, Intermediate temperature solid oxide fuel cells, Chem. Soc. Rev. 37 (2008) 1568–1578.
[7] P.C. Su, C.C. Chao, J.H. Shim, R. Fasching, F.B. Prinz, Solid oxide fuel cell with corrugated thin film electrolyte, Nano Lett. 8 (2008) 2289–2292.
[8] C.C. Chao, C.-M. Hsu, Y. Cui, F.B. Prinz, Improved solid oxide fuel cell performance with nanostructured electrolytes, ACS Nano 5 (2011) 5692–5696.
[9] S.P. Jiang, A review of wet impregnation—an alternative method for the fabrication of high performance and nano-structured electrodes of solid oxide fuel cells, Mater. Sci. Eng. A 418 (2006) 199–210.
[10] Z. Liu, B. Liu, D. Ding, M. Liu, F. Chen, C. Xia, Fabrication and modification of solid oxide fuel cell anodes via wet impregnation/infiltration technique, J. Power Sources 237 (2013) 243–259.
[11] R.J. Gorte, J.M. Vohs, Nanostructured anodes for solid oxide fuel cells, Curr. Opin. Colloid Interface Sci. 14 (2009) 236–244.
[12] K. Joong Yoon, M. Biswas, H.-J. Kim, M. Park, J. Hong, H. Kim, et al., Nano-tailoring of infiltrated catalysts for high-temperature solid oxide regenerative fuel cells, Nano Energy 36 (2017) 9–20.
[13] T. Klemensø, K. Thydén, M. Chen, H.-J. Wang, Stability of Ni–yttria stabilized zirconia anodes based on Ni-impregnation, J. Power Sources 195 (2010) 7295–7301.
[14] P. Keyvanfar, V. Birss, Optimization of infiltration techniques used to construct Ni/YSZ anodes, J. Electrochem. Soc. 161 (2014) F660–F667.
[15] P. Keyvanfar, A.R. Hanifi, P. Sarkar, T.H. Etsell, V.I. Birss, Enhancing the stability of infiltrated Ni/YSZ anodes, ECS Trans. 68 (2015) 1255–1263.
[16] D. Simwonis, F. Tietz, D. Stover, Nickel coarsening in annealed Ni/8YSZ anode substrates for solid oxide fuel cells, Solid State Ion. 132 (2000) 241–251.
[17] Z. Jiao, N. Shikazono, N. Kasagi, Quantitative characterization of SOFC nickel-YSZ anode microstructure degradation based on focused-ion-beam 3D-reconstruction technique, J. Electrochem. Soc. 159 (2012) B285–B291.
[18] J.R. Wilson, W. Kobsiriphat, R. Mendoza, H.-Y. Chen, J.M. Hiller, D.J. Miller, et al., Three-dimensional reconstruction of a solid-oxide fuel-cell anode, Nat. Mater. 5 (2006) 541–544.
[19] P.R. Shearing, J. Golbert, R.J. Chater, N.P. Brandon, 3D reconstruction of SOFC anodes using a focused ion beam lift-out technique, Chem. Eng. Sci. 64 (2009) 3928–3933.
[20] J. Joos, M. Ender, I. Rotscholl, N.H. Menzler, E. Ivers-Tiffée, Quantification of double-layer Ni/YSZ fuel cell anodes from focused ion beam tomography data, J. Power Sources 246 (2014) 819–830.
[21] L. Holzer, B. Münch, B. Iwanschitz, M. Cantoni, T. Hocker, T. Graule, Quantitative relationships between composition, particle size, triple phase boundary length and surface area in nickel-cermet anodes for solid oxide fuel cells, J. Power Sources 196 (2011) 7076–7089.
[22] L. Holzer, B. Iwanschitz, T. Hocker, B. Münch, M. Prestat, D. Wiedenmann, et al., Microstructure degradation of cermet anodes for solid oxide fuel cells: quantification of nickel grain growth in dry and in humid atmospheres, J. Power Sources 196 (2011) 1279–1294.
[23] D. Kennouche, Y.K. Chen-Wiegart, C. Riscoe, J. Wang, S.A. Barnett, Combined electrochemical and X-ray tomography study of the high temperature evolution of Nickel – Yttria Stabilized Zirconia solid oxide fuel cell anodes, J. Power Sources 307 (2016) 604–612.
[24] T. Shimura, Z. Jiao, S. Hara, N. Shikazono, Quantitative analysis of solid oxide fuel cell anode microstructure change during redox cycles, J. Power Sources 267 (2014) 58–68.
[25] T. Shimura, Z. Jiao, N. Shikazono, Evaluation of nickel-yttria stabilized zirconia anode degradation during discharge operation and redox cycles operation by electrochemical calculation, J. Power Sources 330 (2016) 149–155.
[26] G. Brus, K. Miyoshi, H. Iwai, M. Saito, H. Yoshida, Change of an anode's microstructure morphology during the fuel starvation of an anode-supported solid oxide fuel cell, Int. J. Hydrog. Energy 40 (2015) 6927–6934.
[27] M. Kishimoto, M. Lomberg, E. Ruiz-Trejo, N.P. Brandon, Enhanced triple-phase boundary density in infiltrated electrodes for solid oxide fuel cells demonstrated by high-resolution tomography, J. Power Sources 266 (2014) 291–295.
[28] A. Bertei, E. Ruiz-Trejo, F. Tariq, V. Yufit, A. Atkinson, N.P. Brandon, Validation of a physically-based solid oxide fuel cell anode model combining 3D tomography and impedance spectroscopy, Int. J. Hydrog. Energy 41 (2016) 22381–22393.
[29] V.V. Kharton, F.M.B. Marques, A. Atkinson, Transport properties of solid oxide electrolyte ceramics: a brief review, Solid State Ion. 174 (2004) 135–149.
[30] W. Brockner, C. Ehrhardt, M. Gjikaj, Thermal decomposition of nickel nitrate hexahydrate, Ni(NO3)2·6H2O, in comparison to Co(NO3)2·6H2O and Ca(NO3)2·4H2O, Thermochim. Acta 456 (2007) 64–68.
[31] M.R. Somalu, V. Yufit, D. Cumming, E. Lorente, N.P. Brandon, Fabrication and

characterization of Ni/ScSZ cermet anodes for IT-SOFCs, Int. J. Hydrog. Energy 36 (2011) 5557–5566.
[32] C.A. Schneider, W.S. Rasband, K.W. Eliceiri, NIH Image to ImageJ: 25 years of image analysis, Nat. Methods 9 (2012) 671–675.
[33] K.M. Kareh, P.D. Lee, R.C. Atwood, T. Connolley, C.M. Gourlay, Revealing the micromechanisms behind semi-solid metal deformation with time-resolved X-ray tomography, Nat. Commun. 5 (2014) 4464.
[34] S.J. Cooper, A. Bertei, P.R. Shearing, J.A. Kilner, N.P. Brandon, TauFactor: an open-source application for calculating tortuosity factors from tomographic data, SoftwareX 5 (2016) 203–210.
[35] J.C. Russ, R.T. Dehoff, Practical Stereology, 2nd ed, Springer, New York, MA, 2000.
[36] F. Tariq, M. Kishimoto, V. Yufit, G. Cui, M. Somalu, N.P. Brandon, 3D imaging and quantification of interfaces in SOFC anodes, J. Eur. Ceram. Soc. 34 (2014) 3755–3761.
[37] G. Lehmann, Label object representation and manipulation with ITK, Insight J. ⟨http://hdl.handle.net/1926/584⟩ (Accessed 5 April 2017).
[38] T. Hutzenlaub, J. Becker, R. Zengerle, S. Thiele, How coarsening the 3D reconstruction of a porous material influences diffusivity and conductivity values, ECS Electrochem. Lett. 2 (2013) F14–F17.
[39] A. Bertei, H.W. Choi, J.G. Pharoah, C. Nicolella, Percolating behavior of sintered random packings of spheres, Powder Technol. 231 (2012) 44–53.
[40] X. Wang, A. Atkinson, Modeling microstructure evolution of Ni cermet using a cellular automaton approach, J. Electrochem. Soc. 161 (2014) F605–F614.
[41] X. Wang, A. Atkinson, Simulation and prediction of 3-D microstructural evolution and long term performance of Ni-YSZ anode, ECS Trans. 68 (2015) 2867–2873.
[42] X. Wang, Modelling and understanding materials microstructure evolution driven by interface energy, Comput. Mater. Sci. 107 (2015) 1–7.
[43] A. Bertei, F. Tariq, V. Yufit, E. Ruiz-Trejo, N.P. Brandon, Guidelines for the rational design and engineering of 3D manufactured solid oxide fuel cell composite electrodes, J. Electrochem. Soc. 164 (2017) F89–F98.
[44] T. Shimura, Z. Jiao, N. Shikazono, Dependence of solid oxide fuel cell electrode microstructure parameters on focused ion beam - scanning electron microscopy resolution, Int. J. Hydrog. Energy 41 (2016) 22373–22380.
[45] P.R. Shearing, J. Gelb, N.P. Brandon, X-ray nano computerised tomography of SOFC electrodes using a focused ion beam sample-preparation technique, J. Eur. Ceram. Soc. 30 (2010) 1809–1814.
[46] J.R. Wilson, J.S. Cronin, S.A. Barnett, Linking the microstructure, performance and durability of Ni-yttria-stabilized zirconia solid oxide fuel cell anodes using three-dimensional focused ion beam-scanning electron microscopy imaging, Scr. Mater. 65 (2011) 67–72.
[47] M.E. Lynch, D. Ding, W.M. Harris, J.J. Lombardo, G.J. Nelson, W.K.S. Chiu, et al., Flexible multiphysics simulation of porous electrodes: conformal to 3D reconstructed microstructures, Nano Energy 2 (2013) 105–115.
[48] H.-Y. Chen, H.-C. Yu, J.S. Cronin, J.R. Wilson, S.A. Barnett, K. Thornton, Simulation of coarsening in three-phase solid oxide fuel cell anodes, J. Power Sources 196 (2011) 1333–1337.
[49] Z. Jiao, N. Shikazono, Simulation of solid oxide fuel cell anode microstructure evolution using phase field method, J. Electrochem. Soc. 160 (2013) F709–F715.
[50] D. Kennouche, Y.K. Chen-Wiegart, K.J. Yakal-Kremski, J. Wang, J.W. Gibbs, P.W. Voorhees, et al., Observing the microstructural evolution of Ni-Yttria-stabilized zirconia solid oxide fuel cell anodes, Acta Mater. 103 (2016) 204–210.
[51] E.C. Miller, Q. Sherman, Z. Gao, P.W. Voorhess, S.A. Barnett, Stability of nickel-infiltrated anodes in intermediate temperature SOFCs, ECS Trans. 68 (2015) 1245–1254.
[52] Z. Jiao, N. Shikazono, N. Kasagi, Study on degradation of solid oxide fuel cell anode by using pure nickel electrode, J. Power Sources 196 (2011) 8366–8376.
[53] J.T.S. Irvine, D. Neagu, M.C. Verbraeken, C. Chatzichristodoulou, C. Graves, M.B. Mogensen, Evolution of the electrochemical interface in high-temperature fuel cells and electrolysers, Nat. Energy 1 (2016) 15014.
[54] D. Sarantaridis, A. Atkinson, Redox cycling of Ni-based solid oxide fuel cell anodes: a review, Fuel Cells 7 (2007) 246–258.
[55] B. Mandelbrot, How long is the coast of Britain? Statistical self-similarity and fractional dimension, Science 156 (1967) 636–638.
[56] L. Liang, Q. Li, J. Hu, S. Lee, K. Gerdes, L.Q. Chen, Phase field modeling of microstructure evolution of electrocatalyst-infiltrated solid oxide fuel cell cathodes, J. Appl. Phys. 117 (2015) 65105.
[57] R. Davis, F. Abdeljawad, J. Lillibridge, M. Haataja, Phase wettability and microstructural evolution in solid oxide fuel cell anode materials, Acta Mater. 78 (2014) 271–281.
[58] D. Kennouche, Y. Karen Chen-Wiegart, J. Scott Cronin, J. Wang, S.A. Barnett, Three-dimensional microstructural evolution of Ni-yttria-stabilized zirconia solid oxide fuel cell anodes at elevated temperatures, J. Electrochem. Soc. 160 (2013) F1293–F1304.
[59] T.M.M. Heenan, J.J. Bailey, X. Lu, J.B. Robinson, F. Iacoviello, D.P. Finegan, et al., Three-phase segmentation of solid oxide fuel cell anode materials using lab based X-ray nano-computed tomography, Fuel Cells 17 (2017) 75–82.
[60] D.G. Goodwin, H. Zhu, A.M. Colclasure, R.J. Kee, Modeling electrochemical oxidation of hydrogen in Ni-YSZ pattern anodes, J. Electrochem. Soc. 156 (2009) B1004–B1021.
[61] M. Vogler, A. Bieberle-hütter, L. Gauckler, J. Warnatz, W.G. Bessler, Modelling study of surface reactions, diffusion, and spillover at a Ni/YSZ patterned anode, J. Electrochem. Soc. 156 (2009) B663–B672.
[62] P.S. Jørgensen, K. Yakal-Kremski, J. Wilson, J.R. Bowen, S. Barnett, On the accuracy of triple phase boundary lengths calculated from tomographic image data, J. Power Sources 261 (2014) 198–205.

Antonio Bertei obtained his M.Sc. and Ph.D. in Chemical Engineering from the University of Pisa, Italy. After a brief period at the Massachusetts Institute of Technology, he moved to Imperial College London in 2015 thanks to a Marie Skłodowska-Curie Fellowship, where he is currently Research Fellow. His research interests include the physically-based modeling and three-dimensional characterization of electrochemical energy systems and reactive porous media, with special focus on solid oxide fuel cell electrodes and lithium batteries.

Enrique Ruiz-Trejo obtained his M.Sc. in Chemistry from UNAM and his Ph.D. in Materials from Imperial College. He has worked as lecturer at UNAM, Alexander von Humboldt Scholar at the Max Planck Institute for Solid State Research, Senior Scientist at DTU and Research Fellow at the University of St Andrews. Since 2012 he is Research Associate in Fuel Cells and Materials Processing at Imperial College. His areas of interest include materials for energy applications and gas separation membranes, the development of electrodes for fuel cells and the manufacture of metal-ceramic composites.

Kristina Kareh obtained her Ph.D. in Materials Science from Imperial College London in 2013. She then worked as Research Associate in the same university until February 2017, when she joined Nature Publishing as an Associate Editor. Her research interests include in-situ tomography of semi-solid alloys and 3D advanced characterization of solid oxide fuel cell electrodes.

Dr Vladimir Yufit is a Research Fellow at the Department of Earth Science and Engineering at Imperial College London. His broad research interests include development of novel electrochemical energy storage and generation systems and advanced characterization methods at electrode and cell level. He has published over 50 peer-reviewed papers and filed 14 patent applications in the field of electrochemical energy devices and systems. He is a co-founder of IQM Elements Company specializing in development of advanced quantitative imaging methods.

Xin Wang is a research fellow in ceramics in Department of Materials at Imperial College London. He received his Ph.D. from Brunel University in 2001. His research activities include fabrication and characterization of coatings (when he was working in Manchester Materials Science Centre during 2001–2005), laser processing of materials (at Heriot Watt University in 2005), thermal barrier coatings and materials for solid oxide fuel cells (at Imperial College London since 2005). Currently his research interests are on modeling and simulation of materials microstructure, mechanical properties and interfaces of materials for energy application.

Dr. Farid Tariq is a Research Associate at Imperial College London. He received his Ph.D. in 2011 in Materials Science, working on the multi-scale imaging and modeling of hierarchical porous media. Since then, he has specialized in advanced 3D/4D tomography and quantification of complex electrode microstructures for electrochemical energy devices, including fuel cells, batteries and redox flow batteries, with strong collaborations with industrial partners. He is a co-founder of IQM Elements Company specializing in development of advanced quantitative imaging methods.

Professor Nigel Brandon OBE FREng is an electrochemical engineer whose research is focused on electrochemical devices for energy applications, in particular fuel cells, electrolyzers and batteries. He is Director of the UK Hydrogen and Fuel Cell Hub, Co-Director of the UK Energy Storage Hub, and Director of the Sustainable Gas Institute at Imperial College London. He is a founder of the UK fuel cell company Ceres Power.